Prompt and Accurate GRB Source Localization Aboard the Advanced Particle Astrophysics Telescope (APT) and its Antarctic Demonstrator (ADAPT)

Ye Htet,[a,*] Marion Sudvarg,[a] Jeremy Buhler,[a,*] Roger Chamberlain,[a] Wenlei Chen[b] and James Buckley[c] for the APT collaboration

[a] *Washington University in St. Louis, Department of Computer Science & Engineering, St. Louis, MO, USA*

[b] *University of Minnesota, Department of Physics and Astronomy, Minneapolis, MN, USA*

[c] *Washington University in St. Louis, Department of Physics & McDonnell Center for the Space Sciences, St. Louis, MO, USA*

E-mail: htet.ye@wustl.edu, msudvarg@wustl.edu, jbuhler@wustl.edu, roger@wustl.edu, chen6339@umn.edu, buckley@wustl.edu

We characterize the performance of our computational pipeline for real-time gamma-ray burst (GRB) detection and localization aboard the Advanced Particle-astrophysics Telescope (APT) – a space-based observatory for MeV to TeV gamma-ray astronomy – and its smaller, balloon-borne prototype, the Antarctic Demonstrator for APT (ADAPT), whose scientific focus will be the detection of MeV transients. These instruments observe scintillation light from multiple Compton scattering and photoabsorption of gamma-ray photons across a series of CsI detector layers. We infer the incident angle of each photon's first scattering to localize its source direction to a Compton ring about the vector defined by its first two interactions, then intersect rings from multiple photons to identify the GRB's source direction.

We first describe algorithmic improvements that enhance localization accuracy (measured in our previous GEANT4 model of APT) while running in under 0.5 seconds on a low-power ARMv8 processor – fast enough to permit real-time redirection of other instruments for follow-up observations. We then study our pipeline's behavior using a model of the smaller ADAPT detector that incorporates realistic estimates of instrument noise and atmospheric background radiation. Adding *SiPM-based edge detectors*, which gather more light from each scintillation, greatly benefits ADAPT's localization accuracy. We expect that ADAPT can localize normally-incident GRBs of fluence 1 MeV/cm^2 and 1-second duration to within 2-3 degrees at least 68% of the time. The full APT instrument, with its larger detector area and lack of atmospheric background, should be substantially more accurate even on GRBs of fluence as low as 0.1 MeV/cm^2.

38th International Cosmic Ray Conference (ICRC2023)
26 July - 3 August, 2023
Nagoya, Japan

*Speaker

PoS(ICRC2023)956

1. Introduction

The Advanced Particle-astrophysics Telescope (APT) [1] is a concept for a space-based observatory aimed at surveying the entire sky for gamma-ray sources in the MeV to TeV range. APT's goals include real-time localization of gamma-ray bursts (GRBs) to enable follow-up observations of energetic transients by narrow-band instruments within a few seconds of detection. To this end, APT seeks to localize a GRB to within one degree of arc or less within less than a second of its light reaching the instrument. We are interested in capturing even relatively low-fluence GRBs (0.03-1 MeV/cm^2), for which prompt localization will support immediate retargeting of co-located follow-up instruments. This will enable multi-wavelength observations of early gamma-ray afterglows, for which X-ray and UV components may be present within a few seconds [2]. The initial gamma rays produced by events of interest have energies predominantly in the low-MeV range and so interact with APT's detector mainly via multiple Compton scattering.

In prior work [3], we developed a suite of algorithms for real-time GRB detection and localization that can run on low-power computing hardware co-located with APT's detector. We validated these methods using a computational model of the APT detector [4] that we subjected to simulated GRBs using GEANT4 [5]. While GEANT provides accurate physical modeling of photon interactions with the detector, prior work used much simpler approximations for the behavior of APT's front-end electronics, including its silicon photomultipliers (SiPMs) that detect the scintillations produced when gamma rays strike the device. Furthermore, a technology demonstration mission for APT's detector hardware, the Antarctic Demonstrator for APT (ADAPT), is in advanced development with the goal of gathering data from a high-altitude balloon flight in late 2025. ADAPT's detector differs in several critical ways from that envisioned for full APT: it has a much smaller area and is subject to Earth's atmospheric particle background but also has light-gathering features not modeled in our prior work that could materially improve detection accuracy.

In this work, we re-examine the predicted GRB detection performance of ADAPT and APT with the benefit of two years' additional instrument development. We utilize a more detailed model of the detector's optics and electronics [6] that includes sources of noise not captured in our earlier work, as well as a new model of Earth's atmospheric particle background [7] for ADAPT. We account for both algorithmic improvements in our software pipeline and extra light-gathering features of ADAPT, specifically *edge detectors* and *tail counters*. We predict that ADAPT will be able to localize GRBs of fluence around 1 MeV/cm^2 to within 2-3 degrees in well under a second, even at polar angles up to 30 degrees. Finally, we apply our new methods and noise models to estimate the performance of the full APT detector and demonstrate the utility of including edge detectors in its design. APT is predicted to achieve rapid localization with sub-degree accuracy even for fluences as low as 0.1 MeV/cm^2.

2. Background

As described in [1, 4], APT's and ADAPT's detectors consist of multiple layers of tiled CsI(Na) crystal scintillator sheets. Light emitted from energy deposited in the crystal by incoming gamma-ray photons is captured by perpendicular arrays of wavelength-shifting (WLS) optical fibers on the top and bottom of each sheet, which direct it to SiPMs at their ends. The X and Y coordinates of a photon's interaction within the layer are inferred from which fibers are lit, while its Z-coordinate (prior to this work) was inferred from the layer's position in the detector. An interaction's deposited energy is inferred from the amount of light gathered by the fibers and perhaps by additional SiPM-based edge detectors as described in Section 4. A single gamma-ray photon may Compton-scatter one or more times in the detector before it (ideally) is finally photoabsorbed; hence, one photon's interactions with the detector are described by a list of pairs $(\mathbf{r}_i, E_i)$, where $\mathbf{r}_i$ is a 3-vector denoting the ith interaction's coordinates, and E_i is the energy deposited by the photon during this interaction.

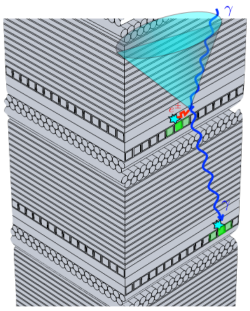

Figure 1: Compton scattering of a gamma ray [1].

We now briefly review our computational approach to GRB localization; a full account is given in [3]. Processing is divided into two phases. In the first phase, the list of interaction positions and energies for each gamma ray is used to reconstruct its trajectory within the detector. Because of the short times between interactions, their order must be inferred by considering multiple possible orderings and choosing the one for which the deposited energies best match the implied scattering angles according to the Compton law. We use an accelerated version of Boggs and Jean's algorithm [8] for this phase, thereby reducing the jth processed gamma-ray photon to a vector $\mathbf{c}_j$ through its first two interactions and an estimate ϕ_j of the angle between the gamma-ray's source direction $\mathbf{s}$ and $\mathbf{c}_j$. The pair $(\mathbf{c}_j, \phi_j)$ defines a *Compton ring* about $\mathbf{c}_j$, as shown in Figure 1, on which the source direction lies.

In the second phase, the individual Compton rings inferred from a burst's detected gamma rays (typically, hundreds to thousands for the fluences considered here) are intersected to infer a single source direction for the GRB. Uncertainties in the centers and angles of the rings make a single common point of intersection unlikely, so we must solve a noisy, overdetermined problem. Our method first uses a small random sample of Compton rings and a likelihood model to infer a rough source direction, then performs iterative least-squares refinement of the source direction using all the rings. Detector noise and incorrect reconstructions (e.g., for gamma rays that leave the detector without being photoabsorbed) mean that the majority of reconstructed Compton rings do not pass near the true source direction, so our localization methods are designed to be robust to noisy inputs. We describe changes to our algorithmic pipeline since [3] in Section 3.

APT vs. ADAPT Instrument: ADAPT's detector is a scaled-down version of that planned for APT. Whereas APT has 20 imaging CsI calorimeter (ICC) layers, each a square 3 m on a side, ADAPT has only 4 ICC layers, each 450 cm on a side. However, in addition to the SiPMs attached to the optical fibers for each layer, ADAPT features *edge detectors* built from additional SiPMs arrayed on two adjacent edges of each layer; these detectors improve calorimetry by capturing optical photons not captured by the fibers. Moreover, ADAPT features four *tail counter* CsI layers, which are instrumented with edge detectors but no optical fibers. An interaction in a tail counter contributes to the total measured energy of the photon but cannot be precisely localized in X or Y.

Unlike APT, which will operate in a Lagrange orbit, ADAPT operates close to the Earth's surface, where a diffuse radiation background from the Earth's limb can interfere with reconstruction of events from actual GRBs. The impact of the background is minimized for GRBs whose source vector is normal to the XY plane of the detector and worsens as the angle with this normal increases.

We investigate the impact of ADAPT's unique additions and challenges in Section 4.

Simulated GRBs: For the experiments described in this work, we simulate gamma-ray bursts (GRBs) in GEANT4 with spectra characterized by a Band function [9]. For each burst, we generate 10^6 gamma-ray photons uniformly across a disk of sufficient size to cover the cross-section of the instrument from any angle. In Section 3, where we evaluate our algorithmic changes since our previous report [3], we use a simulated burst from that prior work, with parameters $\alpha = 0.6$, $\beta = -2.5$ and incident energies from 300 KeV to 10 MeV with a peak at 1 MeV.

For experiments in the remaining sections, we use two Band functions with more realistic parameters $\alpha = -0.5$, $E_{\text{peak}} = 490$ keV, and $\beta \in \{-3.2, -2.1\}$ to capture a range of spectral profiles. Spectral energies are in the range 10 keV – 30 MeV to match the range of energies detectable by the Fermi Gamma-ray Burst Monitor (GBM) [10], from which data the distributions presented in [11] were obtained. In these energy regimes, most gamma rays undergo Compton scattering; occasional pair events are treated as noise by our pipeline. Burst duration is assumed to be one second, with intensity profile over time as described in [6, Section 5].

3. Improvements to Computational Pipeline

The core components of our GRB localization pipeline remain largely similar to those in [3], except for small adjustments to better match the algorithms' assumptions to the detector geometry (in particular, the inter-layer spacing). However, we have made two substantial improvements.

Z-coordinate Estimation: Each scintillation's position $\mathbf{r}_i$ includes X- and Y- coordinates inferred from the WLS fibers associated with the layer in which it occurs. Previously, the Z-coordinate of the scintillation was assumed to be the center of the layer. We have improved this estimate by considering the relative widths (i.e., spans of adjacent lit fibers) of the signals observed in the layer's top and bottom fiber arrays: light from a scintillation further from a given array will propagate across more fibers. Using the known thickness of the CsI tiles, we interpolate a scintillation's Z-coordinate as $z_{\text{pos}} = \frac{\rho}{\rho+1} \cdot h + z_{\text{bot}}$, where $\rho = \frac{w_{\text{bot}}}{w_{\text{top}}}$ is the ratio of the widths, h is the thickness of the CsI layer, and z_{bot} is the absolute Z-coordinate of the bottom of the layer.

Revised Localization: To obtain an initial rough approximation of source direction, we estimate the likelihood of each of a set of possible GRB source directions given an observed set of Compton rings. In our prior work [3, Eqn. 3], the likelihood $\mathcal{L}(\mathbf{s} \mid \mathbf{c}, \phi)$ that a GRB from source direction $\mathbf{s}$ produced an observed Compton ring $(\mathbf{c}, \phi)$ was proportional to $e^{-(\phi-\beta)^2/2\sigma^2}$, where $\beta = \arccos(\mathbf{s} \cdot \mathbf{c})$ and σ is the estimated uncertainty in ϕ. The current pipeline simplifies this likelihood to instead be proportional to $e^{-(\eta-\mathbf{s}\cdot\mathbf{c})^2/2\alpha^2}$, where $\eta = \cos\phi$ and α is the uncertainty in η. Similarly, refinement of $\mathbf{s}$ previously used as inputs all rings for which the angle β was within 3σ of $\arccos(\mathbf{s} \cdot \mathbf{c})$. The current pipeline instead tests whether η is within 3α of $\mathbf{s} \cdot \mathbf{c}$.

These changes use η, not ϕ, consistently throughout localization, since η is the quantity directly inferred for each photon by reconstruction using the Compton law. Empirically, the changes improve localization accuracy and remove computationally expensive arccos calculations from our code.

Validation: To quantify the impact of these changes, we performed a head-to-head comparison of the new pipeline to that described in [3], using the same APT detector model and simulated GRB used in that previous work. We emphasize that this comparison is *only* to enable a fair comparison with our prior work; all validation after this section uses the new, more accurate detector model of [6] and the more realistic sets of GRB parameters described in Section 2.

Table 1: Angular Error of Inferred Source Direction (degrees)

Fluence	Old Pipeline (from [3])		Current Pipeline	
(MeV/cm^2)	68% cnt.	95% cnt.	68% cnt.	95% cnt.
0.03	2.53	4.42	1.65 ± 0.02	2.97 ± 0.04
0.1	1.45	2.32	0.86 ± 0.02	1.46 ± 0.02
0.3	0.87	1.32	0.48 ± 0.01	0.80 ± 0.02
1.0	0.42	0.72	0.24 ± 0.00	0.41 ± 0.01

We tested both pipelines over a range of fluences. For each fluence, we performed 1000 trials with photons randomly selected from our model GRB and report localization accuracy as 68% and 95% *containment* values. A p% containment value means that p% of trials localized the GRB to within the given angular error (in degrees). For the new pipeline, we repeated each experiment ten times to obtain 95% confidence intervals.

Table 1 shows that, at lower fluences, angular error improved by about one degree, while for higher fluences, error was reduced by a factor of ~1.6-1.8. Our changes also slightly improved computation time. We therefore incorporated them into the pipeline used in all subsequent sections.

4. ADAPT-Specific Instrument Improvements and Challenges

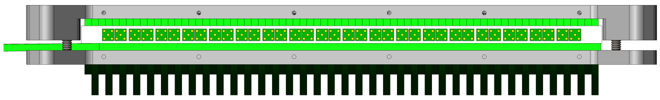

Figure 2: Single-tile edge detector.

Edge Detectors and Tail Counters: ADAPT's smaller effective area, fewer ICC layers, and exposure to atmospheric background radiation are offset by additional detector hardware (not present in the model of APT proposed in [1, 3]) that improves its calorimetry. Each ICC layer consists of a 3×3 layer of CsI(Na) scintillating tiles. Two of the adjacent outward-facing edges of each layer are mirrored, while 3 edge detectors, each multiplexing 36 SiPMs (Fig. 2), are placed on each of the layer's other two edges. The optical and electronic properties of these edge detectors are characterized in [6]. We estimate that, depending on scintillation position, the edge detectors capture 3-11 times as much light as the WLS fibers, which improves estimation of the energy deposited by each gamma-ray interaction with the layer.

Tail counters are constructed identically to the 4 primary ICC layers but have a shorter inter-layer distance and lack WLS fibers. Without the fibers, precise estimates of the spatial positions of each interaction are not possible, and so interactions in the tail counters are not included in the list used by reconstruction. However, the signal distributions across the 6 edge detectors on each layer may be used to localize an interaction to one of the 9 individual CsI tiles. The addition of extra layers also increases the chance of photoabsorption, which in turn increases the chance that the incident photon's *total* energy will be captured – a prerequisite for correct event reconstruction.

ADAPT's improved calorimetry significantly benefits reconstruction of gamma-ray trajectories in the detector and hence GRB localization accuracy. To quantify this benefit, we localized the two newer model GRBs described in Section 2, assuming a source normally incident to ADAPT's detector and a fluence of 1 MeV/cm^2. Figure 3 shows the contributions of edge detectors and tail counters to accuracy, both individually and in combination. Edge detectors alone have a greater benefit, though both together yield the most improvement. These benefits accrue despite the increased electronic noise from multiplexing an edge detector's 36 SiPMs across each of the 6 tile edges in a layer.

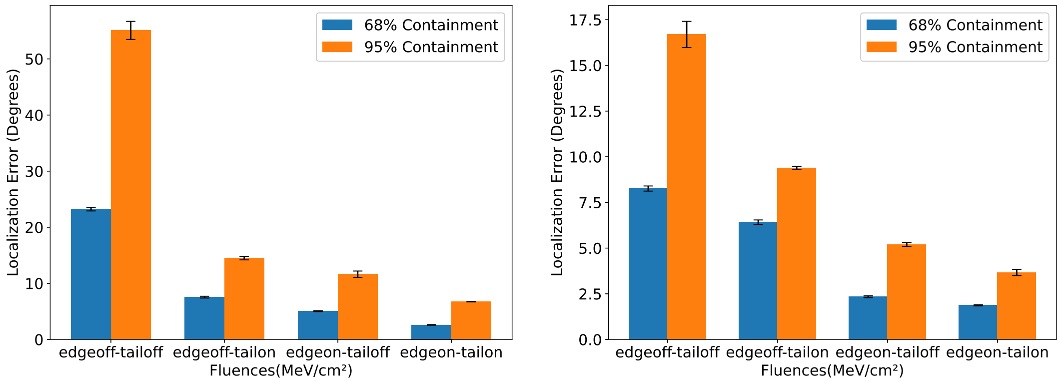

(a) ADAPT: $\beta = -2.1$ **(b)** ADAPT: $\beta = -3.2$

Figure 3: Effect of edge detectors and tail counters on localization accuracy for two model GRBs.

Adding edge detectors (but not tail counters) to the full APT instrument is likely technologically feasible, and our results for ADAPT suggest that they may be beneficial. APT so far lacks the detailed optical modeling described in [6] for ADAPT, in particular the dependence of an interaction's light yield at a layer's edges on its XY coordinates within the layer. Nonetheless, we built a simplified model of APT with edge detectors; this model uses the sophisticated electronics modeling of [6] and accurately models the greater attenuation of light in APT's longer WLS fibers, but it assumes a uniform, position-independent light yield from an interaction in a layer's edge detectors that is equal to the average observed for ADAPT across all possible positions in a layer. Using this enhanced APT model, we observed roughly 3× improvement in 68% localization accuracy for normally incident, 0.1 MeV/cm^2 bursts. Hence, we recommend future consideration of adding edge detectors to APT.

Atmospheric Particle Background: As we plan to deploy ADAPT in the Earth's upper atmosphere, its detector will be exposed to anisotropic background radiation from the Earth's limb. Interactions with background particles will produce Compton rings that are unrelated to any GRB source but will nevertheless be used in localization, decreasing accuracy for low-flux GRBs that are most impacted by the background. To combat this issue, our pipeline employs two strategies to veto background particle events. First, we remove events in which two interactions occur in the same layer, which are more likely to be caused by background particles. Second, we exploit the fact that for ADAPT, detected GRBs can occur only above the horizontal plane. Our software pipeline therefore rejects reconstructed events for which the Compton ring lies entirely below the horizontal.

Table 2: Error with and w/o Background Rejection (degrees)

Fluence	Without Rejection		With Rejection	
(MeV/cm^2)	68% cnt.	95% cnt.	68% cnt.	95% cnt.
0.5	90.03 ± 0.01	91.56 ± 0.05	6.63 ± 0.02	16.33 ± 1.15
1	89.87 ± 0.02	91.46 ± 0.05	2.58 ± 0.04	6.74 ± 0.04
2	1.94 ± 0.05	9.03 ± 1.75	1.54 ± 0.03	3.15 ± 0.11
3	1.34 ± 0.03	4.70 ± 0.18	1.23 ± 0.02	2.33 ± 0.05
4	1.08 ± 0.02	2.46 ± 0.14	1.05 ± 0.02	1.98 ± 0.04

To validate our background rejection strategies, we used the 1-second GRB with $\beta = -2.1$ described in Section 2, assuming normal incidence. One second of background exposure with an energy range of 100 keV to 1 GeV was simulated according to [7]. Table 2 shows that at lower fluences, source events are overwhelmed by the background, and ADAPT could not localize the GRB. However, vetoing likely background particles significantly recovers accuracy. We used our background model and rejection techniques for all subsequent ADAPT experiments in this work.

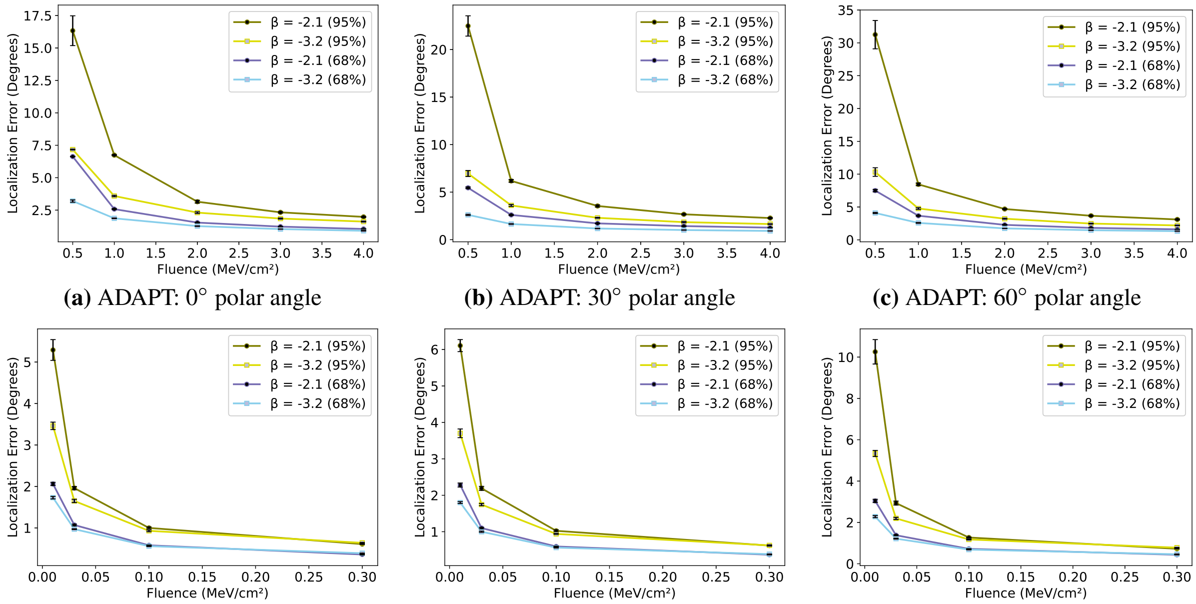

(a) ADAPT: 0° polar angle **(b)** ADAPT: 30° polar angle **(c)** ADAPT: 60° polar angle

(d) APT: 0° polar angle **(e)** APT: 30° polar angle **(f)** APT: 60° polar angle

Figure 4: Localization Accuracy for ADAPT and APT over different incident angles.

5. Localization Results

Accuracy: To test the overall localization accuracy of our pipeline, we model ADAPT's and APT's performance on the two representative GRB spectra described in Section 2. To capture a range of scenarios, we consider polar angles of 0, 30, and 60 degrees; for the off-normal bursts, we consider azimuth angles of both 0 and 45 degrees. At each angle, we simulate bursts with each spectrum over fluences ranging from 0.5 to 4 MeV/cm^2 for ADAPT and 0.01 to 0.3 MeV/cm^2 for APT. The ADAPT detector model is as described in [6] and includes atmospheric background, while the APT model (with edge detector enhancement) is as described in Section 4.

Fig. 4 displays the results of our experiments. Each plot shows localization accuracy as containment values for each burst spectrum; each reported value is the average between the two tested azimuth angles (0° and 45°). For ADAPT, at 1 MeV/cm^2 we expect accuracy within 2-3 degrees 68% of the time for bursts well above the horizon; at 60° from normal, 68% containment accuracy remains within 5 degrees. For APT, we expect to achieve sub-degree localization accuracy at fluences of 0.1 MeV/cm^2 or more and accuracy around one degree at 0.03 MeV/cm^2.

Table 3: Running Times of Pipeline Phases (ms)

Device	Reconstruction		Approximation		Refinement	
	mean	range	mean	range	mean	range
ADAPT	57	56 - 66	209	206 - 218	4	2 - 23
APT	69	67 - 85	365	360 - 402	12	6 - 44

Timing: To verify that our pipeline remains fast enough for prompt GRB localization, we tested its efficiency on the same Raspberry Pi 3B+ device used in [3], a low-power embedded platform with a Cortex-A53 (ARMv8) quad-core, 1.4 GHz, 64-bit CPU and 1 GB of LPDDR2 DRAM. We use this device as a performance proxy for future rad-hardened, low-power processors suitable for orbital deployment. We used our model burst with $\beta = -2.1$ and 1 MeV/cm^2 fluence at normal incidence. We measured elapsed times in milliseconds for event reconstruction, initial approximation of source direction, and iterative least-squares refinement. The experiment was repeated 200 times for each burst, with results shown in Table 3.

Our measurements suggest that both ADAPT and APT can localize typical short GRBs in well under a second. Computation speed was improved by using η directly, as noted in Section 3. Additionally, we halt iteration when the refinement stage converges; at high fluences where convergence is rapid, this helps to balance the cost of processing more events. APT captures more incident photons for a given burst fluence and so has higher, but still adequate, running times.

6. Conclusion

In this work, we have described improvements made to our GRB localization pipeline and its characterization since ICRC 2021 [3]. Our methodological improvements enhance both localization accuracy and computational efficiency, while new optical and electronic models [6] of our instruments provide more realistic accuracy estimates and illustrate the importance of ADAPT's SiPM-based edge detectors and tail counters. For additional realism, we have incorporated the atmospheric background model for ADAPT from [7] and devised methods to reject background particles. Despite the challenges of more accurate noise and background models, we still expect prompt, accurate GRB localization from our near-term ADAPT instrument and likely sub-degree accuracy from the full APT instrument at fluences as low as 0.1 MeV/cm^2. Future work on our pipeline will respond to emerging challenges posed by further device model improvements, particularly in the areas of burst triggering and the optical modeling of full APT.

References

[1] J. Buckley et al., *The Advanced Particle-astrophysics Telescope (APT) Project Status*, in *Proc. of 37th International Cosmic Ray Conference*, vol. 395, pp. 655:1–655:9, July, 2021, DOI.

[2] K. Asano, *Early Gamma-Ray Afterglow from Gamma-Ray Bursts*, in *Proc. of 38th International Cosmic Ray Conference*, vol. 444, pp. 633:1–633:9, July, 2023, DOI.

[3] M. Sudvarg et al., *A Fast GRB Source Localization Pipeline for the Advanced Particle-astrophysics Telescope*, in *Proc. of 37th International Cosmic Ray Conference*, vol. 395, pp. 588:1–588:9, July, 2021, DOI.

[4] W. Chen et al., *The Advanced Particle-astrophysics Telescope: Simulation of the Instrument Performance for Gamma-Ray Detection*, in *Proc. of 37th Int'l Cosmic Ray Conference*, vol. 395, pp. 590:1–590:9, 2021, DOI.

[5] S. Agostinelli, J. Allison, K. Amako et al., *Geant4 — a simulation toolkit*, *Nuclear Instruments and Methods in Physics Research Section A: Accelerators, Spectrometers, Detectors and Associated Equipment* **506** (2003) 250.

[6] M. Sudvarg et al., *Front-End Computational Modeling and Design for the Antarctic Demonstrator for the Advanced Particle-astrophysics Telescope*, in *Proc. of 38th International Cosmic Ray Conference*, vol. 444, pp. 764:1–764:9, July, 2023, DOI.

[7] W. Chen, J. Buckley et al., *Simulation of the instrument performance of the Antarctic Demonstrator for the Advanced Particle-astrophysics Telescope in the presence of the MeV background*, in *Proc. of 38th International Cosmic Ray Conference*, vol. 444, pp. 841:1–841:9, July, 2023, DOI.

[8] S. Boggs and P. Jean, *Event reconstruction in high resolution Compton telescopes*, *Astronomy and Astrophysics Supplement Series* **145** (2000) 311.

[9] D. Band et al., *BATSE observations of gamma-ray burst spectra. I. spectral diversity*, *Astrophys. J.* **413** (1993) 281.

[10] "Overview of the Fermi GBM." `https://fermi.gsfc.nasa.gov/ssc/data/analysis/documentation/Cicerone/Cicerone_Introduction/GBM_overview.html`, Jan., 2020.

[11] L. Nava, G. Ghirlanda, G. Ghisellini and A. Celotti, *Spectral properties of 438 GRBs detected by Fermi GBM*, *Astronomy & Astrophysics* **530** (2011) A21.

Full Authors List: APT Collaboration

Ye Htet[2], Marion Sudvarg[2], Jeremy Buhler[2], Roger D. Chamberlain[2], Wenlei Chen[6], James H. Buckley[7], Corrado Altomare[12], Matthew Andrew[5], Blake Bal[7], Richard G. Bose[7], Dana Braun[7], Eric Burns[4], Michael L. Cherry[4], Leonardo Di Venere[12], Jeffrey Dumonthier[13], Manel Errando[7], Stefan Funk[10], Priya Ghosh[8], Francesco Giordano[9], Jonah Hoffman[7], Zachary Hughes[7], Aera Jung[5], Patrick L. Kelly[6], John F. Krizmanic[13], Makiko Kuwahara[3], Francesco Licciulli[12], Gang Liu[16], Leonarda Lorusso[9], Mario Nicola Mazziotta[12], John Grant Mitchell[11], John W. Mitchell[1], Georgia A. de Nolfo[11], Giuliana Panzarini[15], Richard Peschke[5], Riccardo Paoletti[17], Roberta Pillera[15], Brian Rauch[7], Davide Serini[12], Garry Simburger[7], George Suarez[13], Teresa Tatoli[11], Gary S. Varner[5], Eric A. Wulf[14], Adrian Zink[10], and Wolfgang V. Zober[7]

[1]Astroparticle Physics Laboratory, NASA/GSFC, Greenbelt, MD 20771, USA. [2]Department of Computer Science & Engineering, Washington University, St. Louis, MO 63130-4899, USA. [3]Department of Engineering, University of Hawai‘i at Mānoa, Honolulu, HI 96822, USA. [4]Department of Physics and Astronomy, Louisiana State University, Baton Rouge, Louisiana 70803, USA. [5]Department of Physics and Astronomy, University of Hawai‘i at Mānoa, Honolulu, HI 96822, USA. [6]Department of Physics and Astronomy, University of Minnesota, Minneapolis, MN 55455, USA. [7]Department of Physics and McDonnell Center for the Space Sciences, Washington University, St. Louis, MO 63130, USA. [8]Department of Physics, Catholic University of America, Washington DC, 20064. [9]Dipartimento di Fisica "M. Merlin" dell'Università e del Politecnico di Bari, I-70126 Bari, Italy. [10]Friedrich-Alexander-Universität Erlangen-Nürnberg, Erlangen Centre for Astroparticle Physics, D-91058 Erlangen, Germany. [11]Heliospheric Physics Laboratory, NASA/GSFC, Greenbelt, MD 20771, USA. [12]Istituto Nazionale di Fisica Nucleare, Sezione di Bari, I-70126 Bari, Italy. [13]NASA Goddard Space Flight Center, Greenbelt, MD 20771, USA. [14]Naval Research Laboratory, Washington, DC 20375, USA. [15]Politecnico di Bari, Department of Mechanics, Mathematics and Management, via Orabona, 4, I-70125 Bari, Italy. [16]SLAC National Accelerator Laboratory, 2575 Sand Hill Rd, Mailstop 0094, Menlo Park, CA 94025, USA. [17]Università di Siena and INFN Pisa, I-53100 Siena, Italy.

Acknowledgments

This work was supported by NASA award 80NSSC21K1741 and NSF award CNS-1763503.

PoS(ICRC2023)956